Journal of Sound and Vibration 569 (2024) 118099

Contents lists available at ScienceDirect

Journal of Sound and Vibration

journal homepage: www.elsevier.com/locate/jsvi

Experimental study on the influence of vibration amplitude on the fluid damping of a submerged disk

Greco Moraga [a], Xiang Xia [a], Sergi Roig [a], Carme Valero [a], David Valentín [a], Mònica Egusquiza [a], Lingjiu Zhou [b], Eduard Egusquiza [a], Alexandre Presas [a,*]

[a] Centre for industrial Diagnosis and Fluid Dynamics (CDIF) - Universitat Politècnica de Catalunya, Barcelona, Spain
[b] China Agricultural University, Beijing, China

ARTICLE INFO

Keywords:
Fluid damping
Fluid structure interaction
Vibrating disk
Natural frequency
Mode shape
Resonance

ABSTRACT

Accurate determination of modal parameters for disk-like structures submerged in heavy fluids is a topic of interest in many fields. For instance, some type of hydraulic turbomachinery can be modeled as disk structures due to the similarity in their mode shapes. Although in the recent years many studies have analyzed and correctly predicted the fluid added mass effect on the natural frequencies and mode shapes of these types of structures, it is particularly challenging to determine fluid damping and characterize its most influential effects. In this article, the influence of vibration amplitude on the fluid damping ratio of a submerged disk, when the disk gets close to a rigid wall, is analytically and experimentally studied. Particularly, the first diametrical modes of the disk have been analyzed at different vibration amplitudes and at very small distances away from a rigid surface. The disk is put in a resonant state by means of a piezoelectric patch generating a harmonic excitation and the response is measured by means of a Laser Doppler Vibrometer (LDV). The damping ratio is obtained directly from the vibrating free decay following a sudden stop of the excitation. It is shown that the fluid damping ratio values are related to the vibration amplitude: there is a trend of increasing damping ratio as the amplitude of the vibration increases. This effect is found to be much larger for small distances between the disk and the rigid surface.

1. Introduction

Submerged disk-like structures are relevant in several fields such as mechanical and civil engineering. This is because a disk can be used as a simplified model of many complex structures with similar dynamic response, as has been done for hydraulic turbomachinery, where, the modal behavior of a disk is similar to the modal behavior of critical components such as pump-turbine runners, high head Francis runners or centrifugal pumps [1,2].

One of the most relevant effects on a vibrating structure that is submerged in a heavy fluid is the inertia of the fluid that opposes the motion. This is generally known as added mass, and its effect in structures submerged in heavy fluids, such as water, has been studied extensively by several authors [3–12]. The cited authors investigated the added mass and found that this effect is larger when the structure gets close to a rigid wall. With increasing added mass, the natural frequencies decrease and, therefore, accurate studies of the fluid added mass are of paramount importance in order to avoid structural resonances [13].

* Corresponding author.
E-mail address: alexandre.presas@upc.edu (A. Presas).

https://doi.org/10.1016/j.jsv.2023.118099
Received 5 September 2022; Received in revised form 29 September 2023; Accepted 11 October 2023
Available online 12 October 2023
0022-460X/© 2023 The Authors. Published by Elsevier Ltd. This is an open access article under the CC BY license (http://creativecommons.org/licenses/by/4.0/).

Nomenclature

Symbol

a	disk radius (m) and slope of the straight-line equation $y(t)$ (s^{-1}) only in Section 4.2
A_0	maximum vibration amplitude (mm s^{-1})
$A_{av,i}$	average amplitude of each free decay envelope segment (mm s^{-1})
A_d	amplitude difference (mm s^{-1})
A_{inf-i}	infimum amplitude limit of the free decay envelope segment i
A_{sup-i}	supremum amplitude limit of the free decay envelope segment i
$A(t)$	time dependent free decay envelope (mm s^{-1})
A_{ns}	constant of the mode shape (-)
b	constant value of the straight-line equation $y(t)$ (mm s^{-1})
c_1	proportionally constant (kg s^{-1})
c_2	proportionally constant (kg m^{-1})
C_d	drag coefficient (-)
$C_{d,eq}$	equivalent drag coefficient (-)
C_{ns}	constant of the mode shape (-)
C_{pd}	analog drag coefficient based on pressure difference (-)
d	distance between the disk and the rigid wall (mm)
D	flexural stiffness (Nm) or diameter of the disk (mm), depending on the context
E	Young Modulus (Pa)
E_d	dissipated energy (J)
E_T	total energy of the structure (J)
$E_{T,D}$	total kinetic energy of the disk (J)
$E_{T,F}$	total kinetic energy of the fluid (J)
f	frequency (Hz)
$f(t)$	time dependent force (N)
F_D	drag force (N)
F_d	dissipation force (N)
$F_{p,n}$	force in one wave of a mode n (N)
i	segment number (-)
I_n	second order Bessel function
j	imaginary unit (-)
J_n	first order Bessel function
k_1	coefficient (J^{-1})
k_2	coefficient (-)
$E_{r,F}$	reference kinetic energy of the fluid (J)
$E_{r,D}$	reference kinetic energy of the disk (J)
m	mass of the structure (kg)
M_r	bending momentum (Nm)
n	nodal diameters number (-)
P	pressure (Pa)
$Q_{p,n}$	product of equivalent dynamic pressure and area of the wave of the mode n (N)
r	radial coordinate (m)
Re	Reynolds number (-)
s	nodal circles number (-)
t	time (s)
v	velocity (mm s^{-1})
v_0	reference velocity (mm s^{-1})
V_r	Kelvin–Kirchhoff edge reaction (N)
w	transversal vibration displacement (m)
W_{fluid}	work dissipated by the fluid during one cycle of vibration (J)
W_{ns}	mode shape function (-)
$y(t)$	time dependent straight-line equation in Section 4.2
z	coordinate in direction z (m)

Greek symbol

α	slope of the damping linear trend line (% (mm $s^{-1})^{-1}$)
β_{ns}	added virtual mass incremental
ε_{fluid}	ratio between the energy dissipated by the fluid and the total energy of the structure (-)

ζ	integration variable (-)
θ	angular coordinate (rad)
$\theta 1, \theta 2$	integration limits
λ_{ns}	frequency parameter (1/m)
μ	dynamic viscosity (Pa s)
ν	Poisson modulus (-)
ξ	fluid damping (%)
ξ_0	reference damping (%)
ρ	density (kg m^{-3})
ρ_D	disk material density (kg m^{-3})
ρ_F	fluid density (kg m^{-3})
$\omega_{ns,v}$	natural frequency of an undamped system in vacuum (rad/s)
ω_{ns}	frequency of vibration at the mode *ns* (rad/s)
ρ_D	disk material density (kg m^{-3})
ρ_F	fluid density (kg m^{-3})
$\varnothing$	spatial distribution of the velocity potential
Φ	potential flow velocity field
ψ	mode shape function (-)
ψ_{ns}	radial mode shape function (-)
ψ_θ	angular mode shape function (-)

When a structure vibrates in a viscous fluid, part of the vibration energy is dissipated in the fluid and this is known as added damping or fluid damping. The added damping on disk-like structures has been studied by some authors [14–22]. Yang et al. [14] made a numerical study about an oscillating disk under a steady in-plane current condition and found that the damping coefficient of the oscillating disk is dependent on the Keulegan–Carpenter number. This number has a non-dimensional value that is directly proportional to the velocity amplitude, which describes the relative importance of the drag forces over the inertia force in oscillating bodies. Abazari et al. [15] and Rao et al. [16] conducted an experimental study about an immersed rigid-elastic disk whose oscillation emulates the motion of ocean waves. With this they found a relation between the velocity of the fluid through the disk and the damping coefficient. Vu et al. [17] concluded that the damping coefficient for a disk increases linearly with increasing oscillation amplitude. Similarly, Ann and Faltinsen [18] submerged a perforated rectangular plate into a water tank to make an experimental and numerical study of the added mass and damping. In this study, the plate also oscillated and the added damping was related with the velocity of the water flow passing though the holes of the plate, increasing the damping ratio when the velocity of the water flow was higher. Gauthier et al. [19] made a numerical study about the added damping due to fluid flow over a hydroelectric turbine blade and concluded that the damping due to the water flow over the blade can significantly affect its vibrational behavior. Wang et al. [20] made a numerical analysis of hydrodynamic damping characteristics on a symmetrical hydrofoil, showing that hydrodynamic damping increases when the water flow velocity increases. In line with these results, Roth et al. [21] conducted an experimental study demonstrating that the hydrodynamic damping ratio tended to increase with increasing flow velocity. Finally, Blevins [22] detailed theoretical and experimental results describing flowing water around a flat plate. Each of these studies [14–22] include a mean flow around the structure, either by forcing a flow around the structure or by moving the structure with respect to the fluid. Overall, it can be concluded that when the flow velocity relatively to the structure is higher, the damping is also higher.

A different situation is when a structure vibrates in a standing fluid. In this case, vibrations are small oscillations of all the points of the structure around the equilibrium position. Blevins [22] presented a theoretical model relating the amplitude of vibration with the fluid damping of a cylinder in a still fluid. Valentín et al. [23] demonstrated that the damping ratio value increases when a submerged disk is close to a rigid surface. Vu et al. [24] performed an experimental study of two vibrating rectangular and squared plates. These authors show that the vibration of the plate can cause turbulence in the vicinity of the structure resulting with an abrupt increase in the total damping ratio. They also proposed that the damping ratio of a mode can be considered constant if this turbulence does not appear. They noted that "the damping ratio of a mode is not constant and it can be higher when a noticeable excitation is applied", but formal results about this were not presented. In that study, a non-sensorized hammer was used to excite the plate; hence, the applied force during the impact was not measured. Nayak and Biswal [25] submerged different vibrating structures in a water tank with an oscillating free surface to simulate sea waves, and showed that damping is a function of the water level and the distance of the immersed body to the free surface. A variation of the damping ratio as a function of the distance to the free surface has also been investigated [24,25]. An analytical study of the fluid reaction on a vibrating disk in a viscous medium, considering an infinite water condition showed a trend of decreasing damping with increasing frequency of vibration [26]. These studies [23–26] are mainly focused on relevant parameters affecting the damping, such as the relative position of the disk with respect to rigid and/or free surfaces and exciting frequency.

While many experimental, analytical and numerical analysis about fluid damping have been carried out, relating this parameter with several boundary conditions, only few of them have studied the effect of vibration amplitude on fluid damping. Particularly, fluid damping of a thin fluid film in contact with a vibrating plate has been investigated using fluid films of different thicknesses and vibration amplitudes [27]. The study found that fluid damping of the water film tends to increase with the amplitude of the vibration and with decreasing film thickness. In that case, the fluid film vibrated between the vibrating plate and a free surface. The influence of

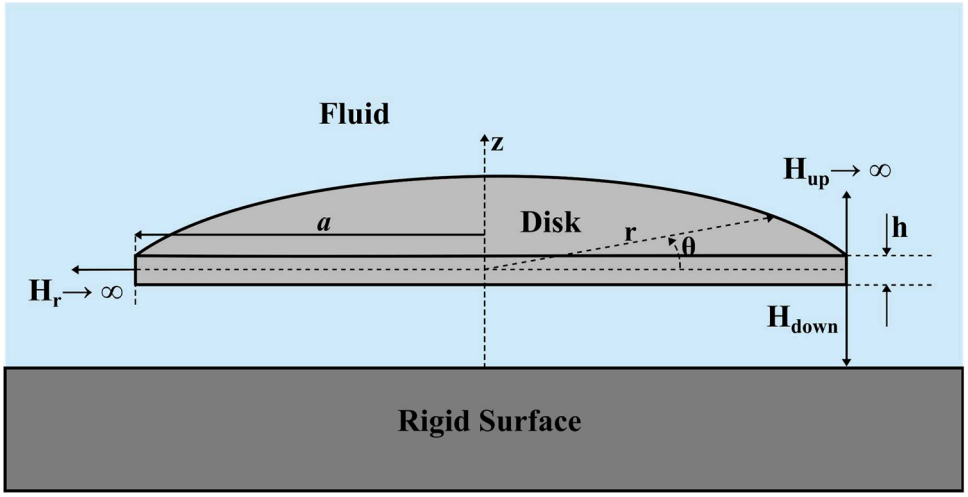


Fig. 1. Scheme of the boundary conditions of the problem.

nearby rigid walls, which has been shown to be an important effect for the added mass were not discussed in that study.

In this study, we determine the fluid damping of a submerged disk-like structure vibrating very close to a rigid wall. The fluid damping ratio is obtained for the several first diametrical modes of the disk. The structure is forced to vibrate with different amplitudes in a resonant state. The position of the disk with respect to the rigid wall is then modified. It is shown that the combined effect of both factors greatly affects the fluid damping of the vibrating structure.

2. Analytical model of a vibrating submerged disk

2.1. Problem statement

In order to study the behavior of the fluid damping in a submerged disk, the problem is reduced to a set of geometrical variables and boundary conditions. In this analysis, a disk with density ρ_D, radius a and thickness h is vibrating at a diametrical mode shape n and is submerged in a heavy fluid, with density ρ_F. Three main distances taken into account are H_{up}, from the upper face of the disk to a rigid surface, H_r from the periphery of the disk to a rigid surface in the radial direction, and H_{down}, from the lower face of the disk to a rigid surface. In order to study the influence of a rigid wall on the dynamic behavior of the disk, the first two distances, H_{up} and H_r, are considered to be infinite. To carry out the following analysis the cylindrical coordinates r, θ and z are considered. The system to study is schematically shown in Fig. 1.

According to Blevins [22], for lightly damped structures vibrating at a resonance frequency, the damping factor is proportional to the ratio of the energy E_d expended in viscous damping per cycle to the total energy of the structure E_T:

$$\xi = \frac{E_d}{4\pi E_T}. \tag{1}$$

In many cases, the energy dissipation mechanism does not follow an ideal viscous damper behavior, so an equivalent damping ratio that expends the same energy per period T can be used instead. For a continuous structure vibrating in a resonance frequency, an equivalent damping ratio can be defined in terms of a viscous damper as:

$$\xi = \frac{\int_0^T \int_0^a \int_0^{2\pi} F_d \dot{w}(r,\theta,t) r d\theta dr dt}{2\pi \int_0^a \int_0^{2\pi} m(r,\theta)[\dot{w}(t)]^2_{max} \psi^2(r,\theta) r d\theta dr}, \tag{2}$$

where, F_d is the dissipation force, $\dot{w}(r,\theta,t)$ is the vibration velocity, $m(r,\theta)$ is the mass per unit area (including the added mass of the surrounding fluid), $\dot{w}(t)_{max}$ is the maximum velocity amplitude and $\psi(r,\theta)$ is the vibration mode shape function. Comparing Eq. (2) with Eq. (1), the upper integral represents the total energy dissipated by the fluid in one cycle and the lower term is 4π times the total kinetic energy spent in the motion of the structure.

2.2. Total kinetic energy of the disk

2.2.1. Mode shapes and natural frequencies in vacuum

Firstly, to calculate the kinetic energy of a submerged disk vibrating a in resonant state, the natural frequencies and mode shapes are determined.

Let us assume the above-described disk to be made of a linearly elastic, isotropic and homogeneous material. If the effects of shear

deformation and rotary inertia are neglected, the equation of motion of the transverse displacement w of the disk is described by Leissa [28] as:

$$D\nabla^4 w + \rho_D h \frac{\partial^2 w}{\partial t^2} = 0, \tag{3}$$

where, D is the flexural stiffness of the disc and ∇^2 is the Laplacian operator in polar coordinates r and θ. D and ∇^2 defined respectively as:

$$D = \frac{Eh^3}{12(1-\nu^2)}, \tag{4}$$

$$\nabla^2 = \frac{\partial^2}{\partial r^2} + \left(\frac{1}{r}\right)\frac{\partial}{\partial r} + \left(\frac{1}{r^2}\right)\frac{\partial^2}{\partial \theta^2}, \tag{5}$$

where, E is the Young modulus and ν is the Poisson modulus.

The solution that satisfies Eq. (3) has the form:

$$w(r,\theta,t) = \sum_{n=0}^{\infty}\sum_{s=0}^{\infty} W_{ns} e^{i\omega_{ns,v}t} \tag{6}$$

and represents the transversal vibration displacement, considering every mode shape. ψ_{ns} is the mode shape function. For a disk, ψ_{ns} is defined by Leissa [28] as:

$$\psi_{ns}(r,\theta) = (A_{ns}J_n(\lambda_{ns}r) + C_{ns}I_n(\lambda_{ns}r))e^{jn\theta}. \tag{7}$$

The subscripts n and s in Eqs. (6) and (7) represent the number of nodal diameters and nodal circles, respectively, in every mode shape. In Eq. (6), j is the imaginary unit number, $\omega_{ns,v}$ is the natural frequency of the plate in vacuum and t is time. In Eq. (7), J_n is the first order Bessel function, and I_n is the modified Bessel function of the first order. A_{ns} and C_{ns} are constants of the mode shape and λ_{ns} is the frequency parameter. A_{ns}, C_{ns} and λ_{ns} are dependent on the boundary conditions [2].

For a free vibrating disk:

$$V_r(r,\theta)|_{r=a} = 0 \tag{8}$$

$$M_r(r,\theta)|_{r=a} = 0. \tag{9}$$

are used as the boundary conditions to solve the equation of motion, where $\boldsymbol{V_r}$ and $\boldsymbol{M_r}$ are the radial Kelvin–Kirchhoff edge reaction and the bending moment, respectively, and are defined as:

$$V_r = -D\left[\frac{\partial}{\partial r}\left(\nabla^2\psi_{ns}(r,\theta)\right) + (1-\nu)\frac{1}{r}\frac{\partial^2}{\partial\theta\partial r}\left(\frac{1}{r}\frac{\partial\psi_{ns}(r,\theta)}{\partial\theta}\right)\right], \tag{10}$$

$$M_r = -D\left[\frac{\partial^2\psi_{ns}(r,\theta)}{\partial r^2} + \nu\left(\frac{1}{r}\frac{\partial\psi_{ns}(r,\theta)}{\partial r} + \frac{1}{r^2}\frac{\partial^2\psi_{ns}(r,\theta)}{\partial\theta^2}\right)\right]. \tag{11}$$

Once λ_{ns} is determined, the circular frequency $\omega_{ns,v}$ can be obtained with the following equation:

$$\omega_{ns,v} = \sqrt{\frac{\lambda_{ns}^4 D}{h\rho_D}}. \tag{12}$$

2.2.2. Added mass effect

When a vibrating structure is submerged in a still heavy fluid at rest, a motion of the fluid is induced by this one. Then, this structure not only move its own mass but a portion of mass of fluid too. To obtain the kinetic energy of the submerged disk, the total moving mass (including the water fluid added mass) needs to be determined.

Even though natural frequencies considerably decrease when the structure is submerged in a heavy fluid, such as water, the mode shape barely changes after the submersion [3,29]. Considering this, a relationship between the natural frequencies in vacuum and the frequencies of the free vibration of the submerged structures is shown by Amabili et al. [3] as follows:

$$\omega_{ns} = \frac{\omega_{ns,v}}{\sqrt{1+\beta_{ns}}}. \tag{13}$$

Here, $\boldsymbol{\omega_{ns}}$ is the free vibration frequency of the submerged structure, $\boldsymbol{\omega_{ns,v}}$ is the natural frequency of the structure in vacuum and $\boldsymbol{\beta_{ns}}$ is the added virtual mass incremental (AVMI) factor. $\boldsymbol{\beta_{ns}}$ is defined as the ratio between the kinetic energy of the fluid $\boldsymbol{E_F}$, due to the vibration of the disk, and the kinetic energy of the vibrating disk itself $\boldsymbol{E_D}$. Then:

$$\beta_{ns} = \frac{E_F}{E_D}. \tag{14}$$

To obtain the kinetic energy of the fluid, the movement of the fluid in both upper and lower regions of the disk has to be determined. Similar to other studies [3,30–32] for the calculation of $\boldsymbol{\beta}_{ns}$, the fluid is considered inviscid, incompressible and irrotational. Also, the movement of the fluid is assumed to be only due to the vibration of the disk. Considering the mentioned assumptions, the movement of the fluid can be described with:

$$\Phi(r,\theta,z,t) = \varnothing(r,z)e^{in\theta}\dot{g}(t), \tag{15}$$

where, $\varnothing$ is the spatial distribution of the velocity potential, $g(t) = e^{i\omega_{ns}t}$, with ω_{ns} as the frequency of the mode ns of the submerged disk and $\dot{g}(t)$ the derivative of $g(t)$ with respect to the time. This type of flow satisfies the Laplace equation described by Φ:

$$\nabla^2\Phi = 0. \tag{16}$$

After substituting Eq. (15) in Eq. (16) the following equation is obtained:

$$\frac{\partial^2\varnothing}{\partial r^2} + \frac{1}{r}\frac{\partial\varnothing}{\partial r} + \frac{\partial^2\varnothing}{\partial z^2} - \frac{n^2}{r^2} = 0. \tag{17}$$

To determine $\varnothing$, the rigid walls in the upper and lower rigid surfaces are considered, and so the non-penetration boundary conditions

$$\left.\frac{\partial\varnothing}{\partial z}\right|_{z=H_{up}} = 0, \tag{18}$$

$$\left.\frac{\partial\varnothing}{\partial z}\right|_{z=\boldsymbol{H_{up}}} = 0, \tag{19}$$

and

$$\left.\frac{\partial\varnothing}{\partial z}\right|_{z=0} = \frac{Dw}{Dt}, \tag{20}$$

where, $\frac{Dw}{Dt}$ is the material derivate of the disk vibration displacement. It is important to remark that the boundary condition of Eq. (18) is only used for the calculation of the potential flow in the upper region of the fluid and the distance to an upper wall is considered to be infinite.

To determine the spatial distribution of the velocity potential, it is useful to apply the Hankel transform to $\varnothing$, as shown by Amabili et al. [3]:

$$\varnothing(\boldsymbol{r},z) = \int_0^\infty \boldsymbol{\zeta}[\boldsymbol{B}(\boldsymbol{\zeta})\boldsymbol{e}^{-\zeta z} + \boldsymbol{C}(\boldsymbol{\zeta})\boldsymbol{e}^{\zeta z}]\boldsymbol{J_n}(\boldsymbol{\zeta r})\boldsymbol{d\zeta}, \tag{21}$$

where, $B(\zeta)$ and $C(\zeta)$ are functions dependent on the boundary conditions and ζ is an integration variable.

Once the functions $B(\zeta)$ and $C(\zeta)$ are determined by using the boundary conditions of this problem, as shown by Louyot et al. [2] and Amabili et al. [3] and making $\varnothing$ to satisfy Eq. (17), the expression of potential flow for both upper and lower regions can be obtained:

$$\varnothing_{up}(r,z) = -a\omega_{ns}\int_0^\infty H(\eta)J_n(\eta\hat{r})\left[\frac{e^{-\eta\hat{z}} + e^{\eta\left(\hat{z}-2\hat{H}_{up}\right)}}{1-e^{-2\eta\hat{H}_{up}}}\right]d\eta, \tag{22}$$

$$\varnothing_{down}(r,z) = -a\omega_{ns}\int_0^\infty H(\eta)J_n(\eta\hat{r})\left[\frac{e^{-\eta\hat{z}} + e^{\eta(\hat{z}-2\hat{H}_{down})}}{1-e^{-2\eta\hat{H}_{down}}}\right]d\eta, \tag{23}$$

where, $\hat{r} = \frac{r}{a}$, $\hat{z} = \frac{z}{a}$, $\hat{H}_{up} = \frac{H_{up}}{a}$, $\hat{H}_{down} = \frac{H_{down}}{a}$ and $\eta = r\zeta$, $H(\eta) = \int_0^1 \hat{r}\psi_{r,ns}(\hat{r})J_n(\eta\hat{r})d\hat{r}$ and $\psi_{r,ns}$ is the radial deformation function at each mode ns defined as:

$$\psi_{r,ns} = A_{ns}J_n(\lambda_{ns}r) + C_{ns}I_n(\lambda_{ns}r). \tag{24}$$

After the potential flow is obtained for both regions of the disk, the kinetic energy of the fluid E_F in the vicinity of the wall (at $\hat{z} = 0$) can be obtained with the following expression:

$$E_F = -\frac{1}{2}\rho_F a^2 \psi_\theta \int_0^1 \left[\varnothing_{sup}(\hat{r},0) + \varnothing_{inf}(\hat{r},0)\right]\psi_{r,ns}(\hat{r})\hat{r}d\hat{r}, \tag{25}$$

where $\psi_\theta = 2\pi$ if $n = 0$ and $\psi_\theta = \pi$ if $n > 0$, as the result of the integration over θ [3].

The kinetic energy of the disk E_D is defined just by the motion of the disk:

$$E_D = \frac{1}{2}\rho_D a^2 \psi_\theta h \int_0^1 \psi_{r,ns}(\hat{r})^2 \hat{r}d\hat{r}. \tag{26}$$

After both reference energies, fluid and disk, are obtained, the AVMI factor can be calculated:

$$\beta_{ns} = \frac{E_F}{E_D} = \frac{-\rho_F \int_0^1 \left[\varnothing_{sup}(\hat{r},0) + \varnothing_{inf}(\hat{r},0)\right]\psi_{r,ns}(\hat{r})\hat{r}d\hat{r}}{\rho_D h \int_0^1 \psi_{r,ns}(\hat{r})^2 \hat{r}d\hat{r}}. \tag{27}$$

Finally, the total kinetic energy of a submerged disk in presence of a nearby rigid wall is defined by the kinetic energy of the disk including the added mas of water as:

$$E_T = \frac{1}{2}(1+\beta_{ns})\pi\rho_D h\omega_{ns}^2 a^2 \int_0^1 \psi_{ns}^2(\hat{r})\hat{r}d\hat{r}, \tag{28}$$

2.3. Energy dissipated by the fluid

In General, the energy dissipated can be defined for one vibration mode as the work done by the dissipation force:

$$E_d = \int_0^{one\ cycle} |F_d|dw = \int_t^{t+T} |F_d \dot{w}|dt, \tag{29}$$

where F_d and dw are the dissipative force and displacement differential, respectively, T is the period of the oscillation and $\dot{w}$ is the vibration velocity. Then, for a continuous structure, oscillating at its natural frequency in one mode and in one direction, the dissipation energy is given by Blevins [22]:

$$E_d = \int_0^T \int_0^a \int_0^{2\pi} |F_d \dot{w}(r,\theta,t)| r d\theta dr dt. \tag{30}$$

On the other side, it is possible to use Eq. (2) to obtain the dissipated energy by an equivalent viscous damping in terms of the total kinetic energy of the disk and the damping ratio as:

$$E_d = 2\pi^2 \xi (1+\beta_{ns})\rho_D h A_n^2 \omega_{ns}^2 a^2 \int_0^1 \psi_{ns}^2(\hat{r})\hat{r}d\hat{r}. \tag{31}$$

In still fluid, the main dissipative force is the drag. This force is produced by the viscous shearing of the fluid at the surface of the structure and the flow separation due to the differences of pressure between the structure surfaces. The drag force is defined as [22,33]:

$$F_D = -\frac{1}{2}\rho_F |\dot{w}(r,\theta,t)|\dot{w}(r,\theta,t) A_d C_D, \tag{32}$$

where, C_D represents the drag coefficient and the term A_d represent the projected area of the body, normal to the displacement of the structure. The energy dissipated by this force can be obtained with [34]:

$$E_d = \int_0^{A_d}\int_0^T \left| -\frac{1}{2}\rho_F C_D |\dot{w}(\hat{r},\theta,t)^3| \right| dt dA_d = \frac{1}{2}\rho_F C_D \int_0^{A_d}\int_0^T |\dot{w}(\hat{r},\theta,t)^3| dt dA_d. \tag{33}$$

If the velocity is defined as: $\dot{w}(\hat{r},\theta,t) = A_n \psi_{r,ns}(\hat{r})\psi_\theta(\theta)\dot{g}(t)$, the dissipated energy by the drag force has the form:

$$E_d = \frac{1}{2}\rho_F a^2 C_D \int_0^1 \int_0^{2\pi} \int_0^T |A_n \psi_{r,ns}(\hat{r})\psi_\theta(\theta)\dot{g}(t)|^3 \hat{r} dt d\theta d\hat{r}. \tag{34}$$

In order to know the resistance of the fluid to the motion of the structure, an equivalent drag coefficient $C_{D,\ eq}$ can be calculated equating Eqs. (31) and (34):

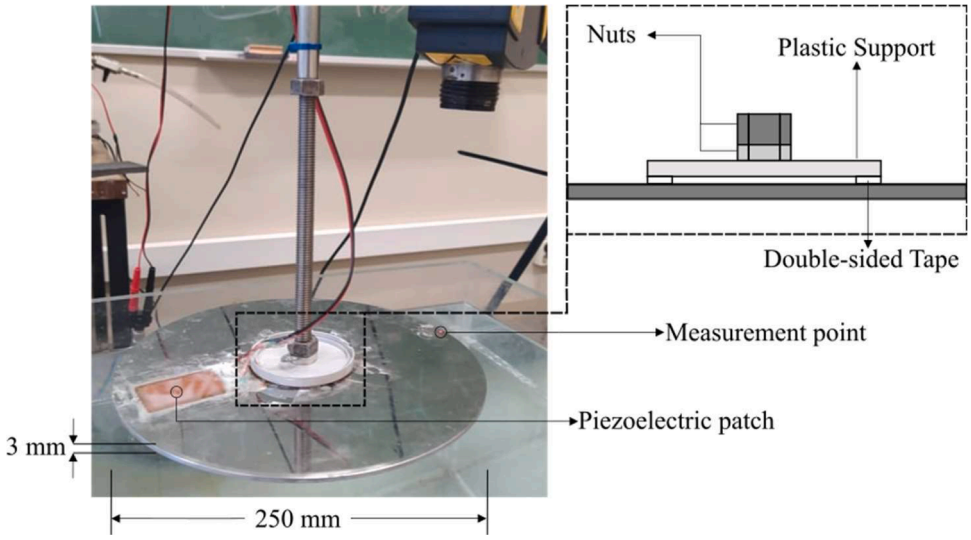


Fig. 2. Disk setup and instrumentation used.

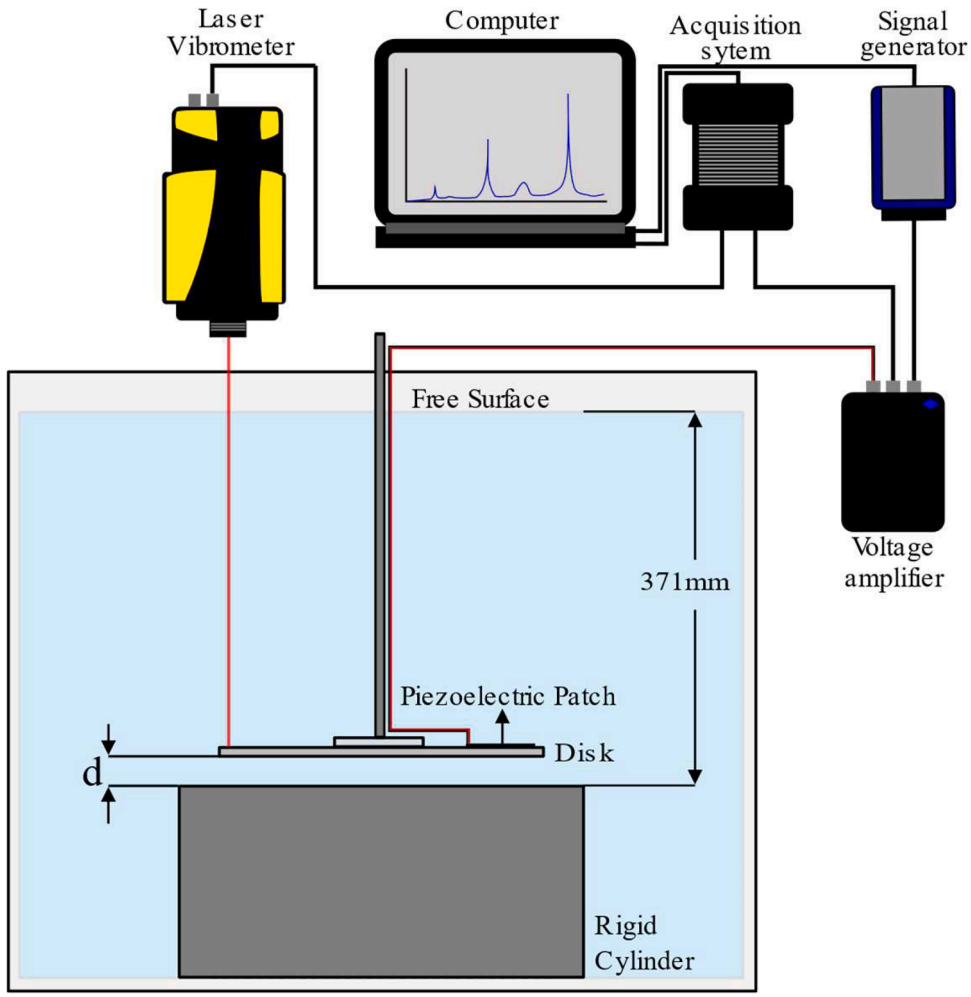


Fig. 3. Scheme of the experimental setup.

Table 1
Summary of the configurations tested as a function of the distance to the rigid wall.

Configurations	
d (mm)	d/D (%)
118	47.2
18	7.2
10	4
5	2
2	0.8

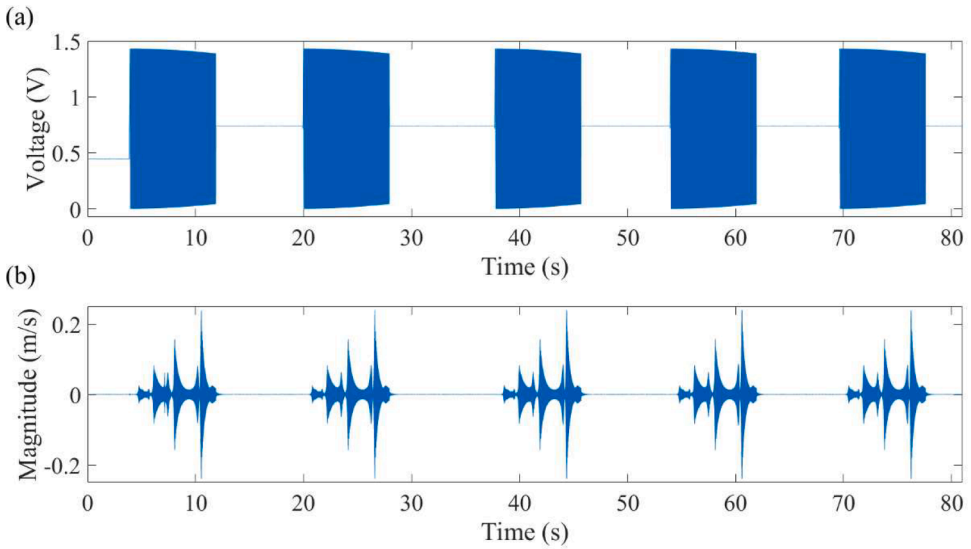


Fig. 4. Chirp test: (a) Excitation Signal (PZT) and (b) Vibration signal (LDV).

$$2\pi^2\xi(1+\beta_{ns})\rho_D h A_n^2\omega_{ns}^2 a^2\int_0^1\psi_{ns}^2(\hat{r})\hat{r}d\hat{r} = \frac{1}{2}\rho_F a^2 C_{D,eq}\int_0^1\int_0^{2\pi}\int_0^T\left|A_n\psi_{r,ns}(\hat{r})\psi_\theta(\theta)\dot{g}(t)\right|^3\hat{r}dtd\theta d\hat{r}, \tag{35}$$

so:

$$C_{D,eq} = \frac{\omega_{ns}^2 2\pi^2\xi(1+\beta_{ns})\rho_D h\int_0^1\psi_{ns}^2(\hat{r})\hat{r}d\hat{r}}{\frac{1}{2}\rho_F A_n\int_0^1\int_0^{2\pi}\int_0^T\left|\psi_{r,ns}(\hat{r})\psi_\theta(\theta)\dot{g}(t)\right|^3\hat{r}dtd\theta d\hat{r}}. \tag{36}$$

Thus, the total drag force in the structure can be obtained using Eq. (36) in Eq. (32).

3. Experimentation performed

3.1. Experimental setup

For this study, a stainless steel disk with a thickness of 3 mm and a diameter of 250 mm is used. A steel beam is used to prevent possible large oscillations of the disk (very low frequency motions) in the axial direction. The steel beam has been carefully attached to the disk with pieces of double-sided tape that are much less rigid than the stainless steel (Fig. 2).

The disk is submerged in a tank full of water with varying distances to the rigid wall, as shown schematically in Fig. 3. The upper surface of a stiff cylinder (diameter = 350 mm, height = 250 mm) is used as a rigid wall. The walls of the tank are far away enough from the disk to not influence its modal behavior.

Table 1 shows a summary of the configurations that have been tested. In short, the distance disk-rigid wall is changed from experiment to experiment. It has been experimentally verified that the natural frequencies of the disk do not change for submergence levels h between 250 mm and 300 mm which corresponds respectively to d equals to 118 mm and 68 mm. Within this range, the disk can be considered as vibrating in an infinite water medium as the natural frequencies remain constant and, therefore, there are no relevant effects of the free surface or the rigid surface (upper face of the rigid cylinder). Hence, the configuration $d = 118$ mm or $d/D =$

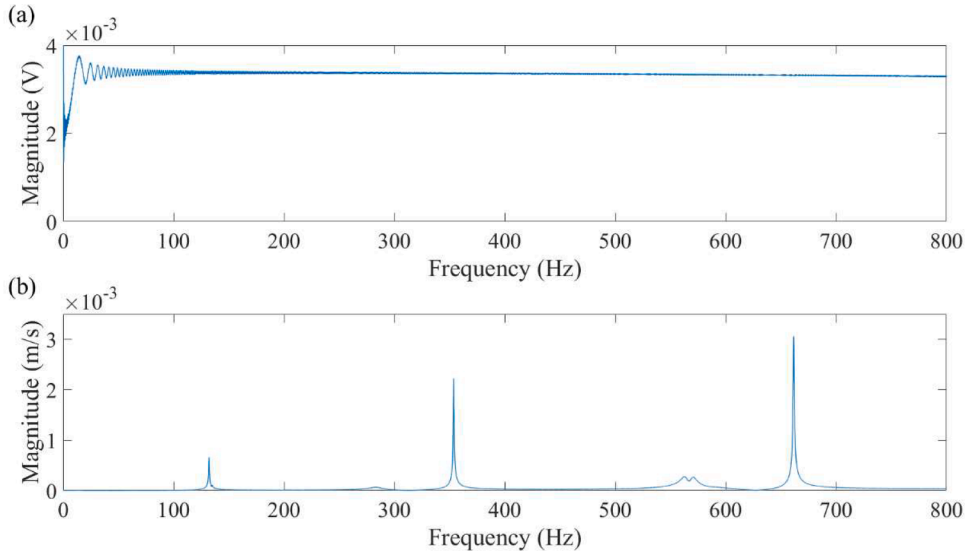


Fig. 5. Frequency spectrum for d/D = 47.2 %: (a) PZT and (b) LDV.

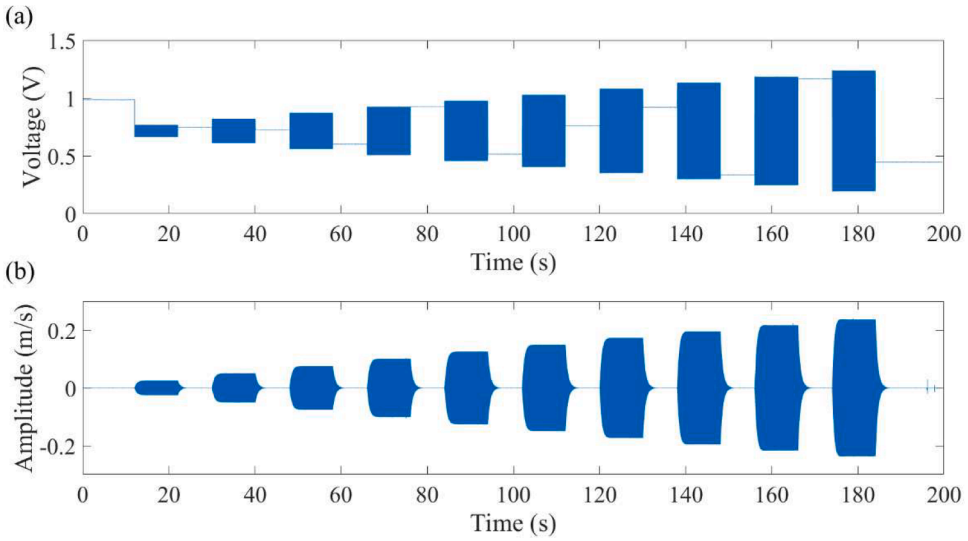


Fig. 6. Pure cosine excitation of the disk at increasing amplitudes: (a) Excitation Signal (PZT) and (b) Response signal (LDV).

47.2 % will be referred to as the "infinite water" case. The remaining configurations are very close to the rigid surface where an increased added mass and fluid damping is expected.

To carry out the following experiments and accurately measure the fluid damping, the disk needs to be excited without disturbing the surrounding fluid. For this, a light piezoelectric patch (P-876.A12 DuraAct Patch Transducers, 3.5 g, (PZT)) is attached to the disk. The excitation signal is generated by means of a signal generator (National Instruments 9263) and is sent to a signal amplifier (OEM835) that activates the piezoelectric patch (PZT) in the desired voltage range (−100 to 250 V). In order to measure the dynamic response of the disk without disturbing the surrounding flow, a Laser Doppler Vibrometer (Polytec PDV 100 (LDV)) with a sensitivity of 8 mV $(\text{mm s}^{-1})^{-1}$ is used (see Fig. 2).

Both excitation and response signals are acquired with a Brüel & Kjær Type 3053-B-120 acquisition system with a sampling frequency of 32,769 samples s^{-1}. A scheme of the instrumentation connection is shown in Fig. 3.

3.2. Experiments

3.2.1. Chirp test

For each of configurations listed in Table 1, the first step is to know the natural frequencies and mode shapes of the disk. For this

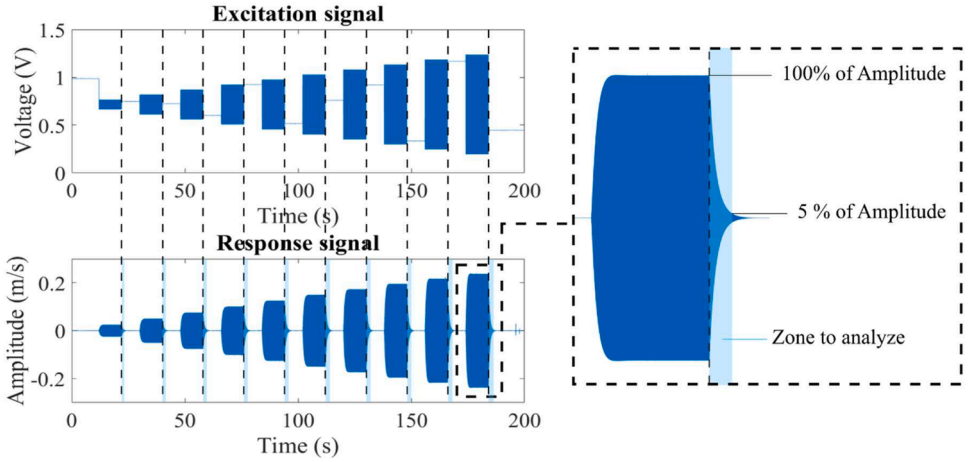


Fig. 7. Free decay identification and zone to analyze.

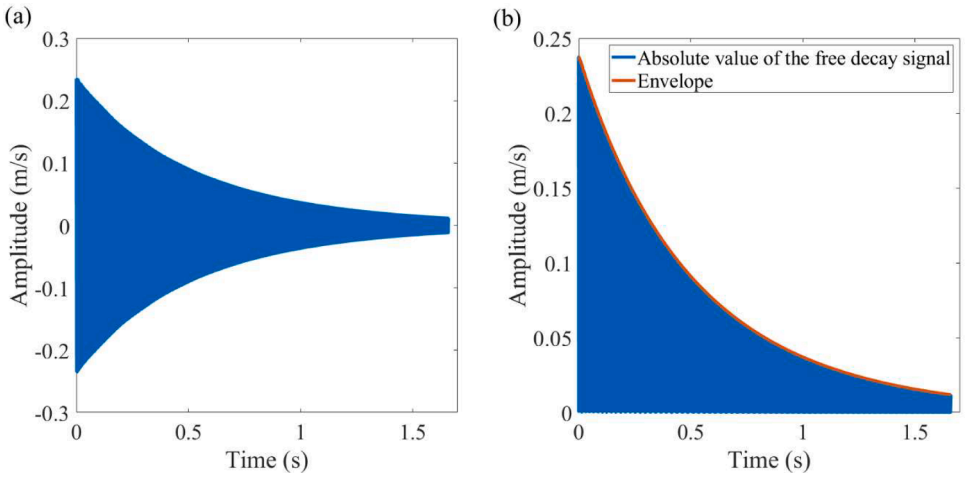


Fig. 8. Free decay: (a) Measured free decay and (b) Absolute value of the measured free decay.

purpose, a chirp frequency signal is sent from the signal generator to the PZT in order to excite the disk. Five excitations are generated from 0 to 1600 Hz in 8 s, and both excitation (PZT) and response (LDV) signals are acquired (Fig. 4).

The vibration signals are processed in order to obtain the natural frequencies of the disk. Every excitation lasts 8 s (Fig. 4a) such that the signals are windowed with transient windows slightly longer than the excitation (in this case 8.5 s). Even so, the total window time is 16 s, making the frequency resolution 0.0625 Hz. Then, the Fast Fourier Transformation (FFT) is applied to each window and finally, a resulting spectrum is obtained by averaging the five excitations performed. Fig. 5a shows an example of an averaged spectrum for the PZT, as well as the frequency range excited, and Fig. 5b shows the averaged spectrum for the LDV. Three clear resonant peaks can be seen in all the configurations, which are the first diametrical modes of the disk (modes with respectively 2, 3, 4 nodal diameters and 0 nodal circles). These three vibration modes are considered in this paper.

3.2.2. Resonance excitation with increasing amplitude

Once the precise values of the natural frequencies of interest are known, the disk is excited at each of these frequencies with a harmonic excitation (pure cosine wave). Every harmonic excitation lasts for 10 s in order to assure a steady vibrating behavior of the disk at the end of the cycle. After this, the excitation is suddenly stopped and the disk exhibits a free decay response governed by the total damping. When the free decay response finishes, the disk remains still for 8 s. After this, the disk is excited again with a larger excitation amplitude. This procedure is repeated 10 times. In the response signal (Fig. 6b), it is possible to see that the free decay is generated after each excitation stops (Fig. 6a).

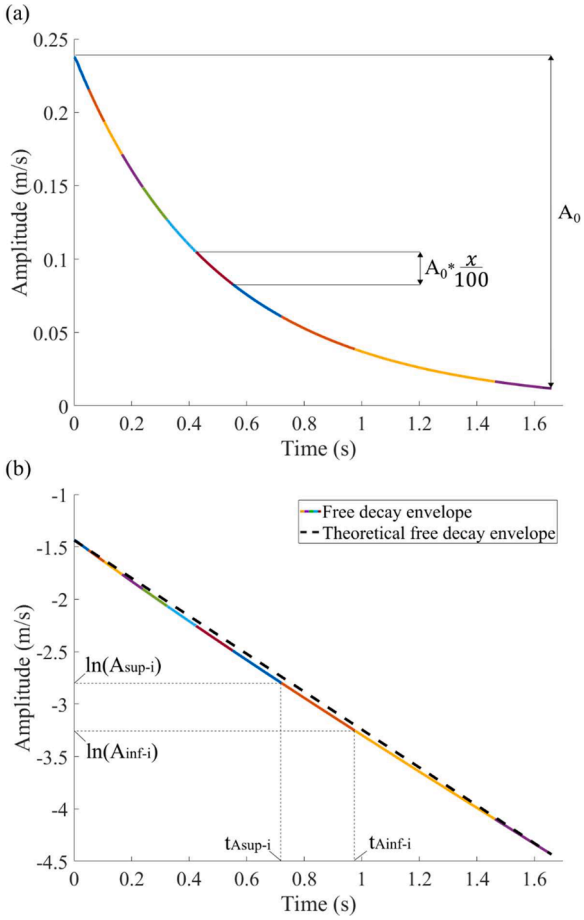


Fig. 9. Envelope of the free decay: (a) Exponential decay in linear scale and (b) Comparison between the envelope of the decay in logarithmic scale and a straight line (theoretical decay for constant damping).

4. Fluid damping extraction from the experimental data

4.1. Envelope characteristic of the free decay

The experimental data collected is processed in a code written in MATLAB R2020b to obtain precise estimations of the total damping for each decay. The data processing is explained as follows. As an example of the explanation, the mode $n = 3$ in infinite water is used (Fig. 7).

In order to have a clean free decay response, the response signals obtained with the LDV need to be filtered. The code filters the data with a bandpass filter centered on the excited frequency and with a bandwidth of ± 50 Hz. It is checked that the shape of the free decay zone is not modified after applying these filters.

For each free decay, the code detects the start and the end of the zone to be analyzed. As schematically shown in Fig. 7, the region to study has a time length that depends on the relative amplitudes. The left limit of this region is given by the maximum amplitude of the excitation at the moment when the excitation stops (maximum amplitude during the forced steady vibration). The right limit is set as 5 % of the maximum amplitude of the steady vibration. In this way, a free decay response is obtained (Fig. 8a). A single envelope characteristic is obtained by calculating the absolute value of the signal (Fig. 8b).

4.2. Damping calculation from the envelope characteristic

For vibration modes that feature well-separated frequencies, each vibrating mode can be considered as a single degree of freedom system (SDOF). The free response characteristic of this system is when the force is equal to zero is given by:

$$w(t) = A_0 e^{-\xi\omega_n t} \sin\left(\omega_n \sqrt{1-\xi^2}\ t\right), \tag{37}$$

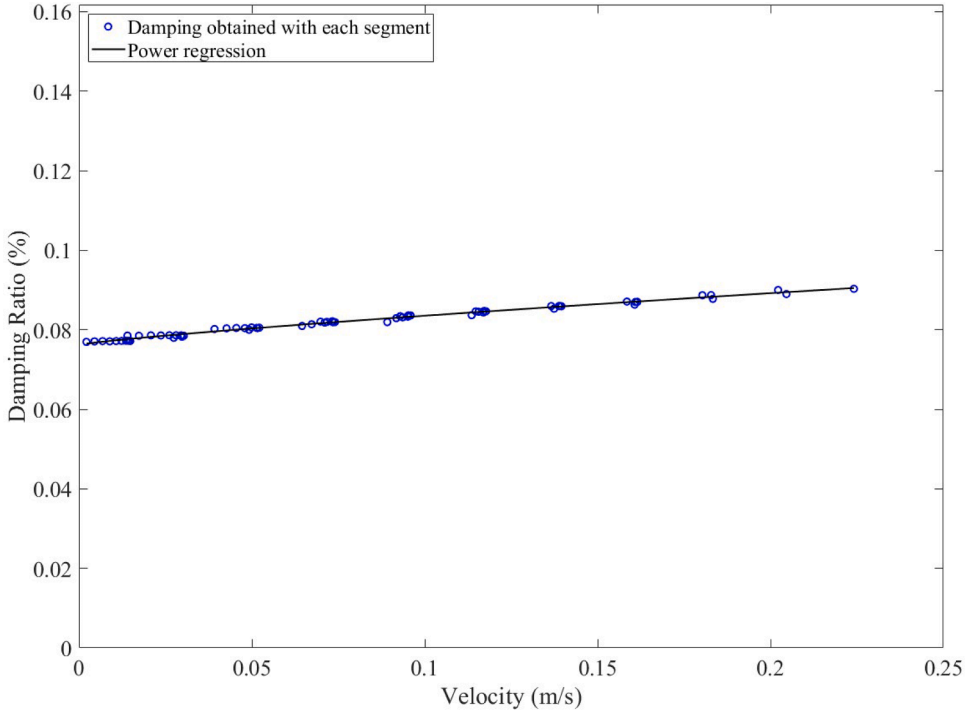


Fig. 10. Total Damping ratio and amplitude of vibration. Example for $n = 3$ and $d/D = 47.2$ %.

where, A_0 is the maximum amplitude, ξ is the damping ratio, ω_n is the natural frequency of the undamped SDOF, and t is the time. This function is a sine wave with a frequency $\omega_n\sqrt{1-\xi^2}$ and decaying amplitude. The positive envelope of this decaying behavior is given by

$$A(t) = A_0 e^{-\xi\omega_n t}. \tag{38}$$

Using logarithms, Eq. (38) can be written as

$$\ln(A(t)) = -\xi\omega_n t + \ln(A_0). \tag{39}$$

Eq. (39) in a logarithmic scale is a straight line with the form

$$y(t) = -at + b, \tag{40}$$

where,

$$a = \xi\omega_n, \text{ and } b = \ln(A_0), \tag{41}$$

while the dimensionless damping ratio is given by

$$\xi = \frac{a}{\omega_n} \tag{42}$$

Note that with this procedure, the damping ratio ξ can be theoretically obtained with an arbitrary part of the envelope characteristic. Furthermore, by differentiating Eq. (38) it can be shown that the damping can be calculated in the same way with the envelope of the velocity characteristic.

4.3. *Damping extraction for different amplitudes of vibration*

Fig. 9a show the envelope characteristic experimentally obtained for the case shown in Fig. 8 (linear scale). Fig. 9b shows the same envelope characteristic in a logarithmic scale. As a reference, a dashed line that follows a straight line is also shown in the same figure. If the measured curve would follow the dashed line, it would mean that the damping ratio does not change with the amplitude (slope $a = \xi\omega_n$ in Eq. (40) is constant). For the shown case, it can be clearly seen that the measured free decay does not follow the dashed line, which indicates that the damping ratio is changing.

To analyze the changes of the damping ratio, the free decay envelope is divided into different segments in order to calculate the damping ratio at different amplitude values. In the example shown in Fig. 9a, 11 segments with 9 % of the maximum amplitude have

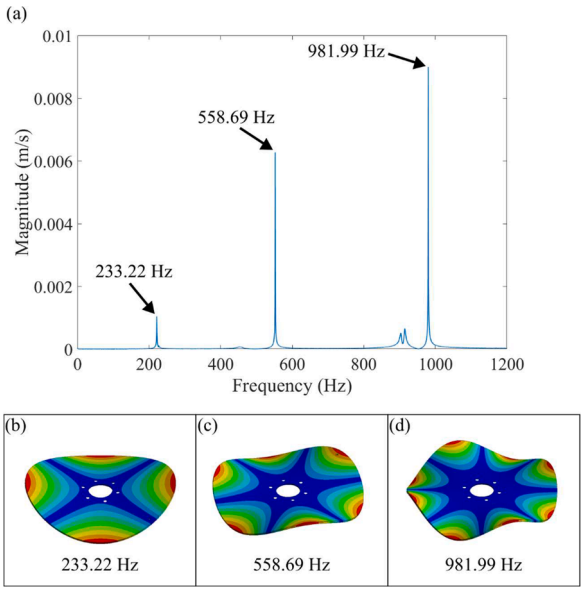


Fig. 11. Natural frequencies and Mode shapes: (a) Frequency spectrum obtained experimentally, (b) $n = 2$ mode shape obtained by simulation, (c) $n = 3$ mode shape obtained by simulation and (d) $n = 4$ mode shape obtained by simulation.

been taken. Then, the slope of each segment is calculated, from which the damping ratio is obtained. Formally written, each segment is defined by an amplitude difference A_d

$$A_d = A_0 \cdot \left(\frac{x}{100}\right), \tag{43}$$

where, x is the percentage selected for the division.

A segment i will be delimited by Asup-i, Ainf-i and the corresponding times $t_{\text{Asup-i}}$, $t_{\text{Ainf-i}}$. With these parameters, the damping of the segment i can be calculated as

$$\xi_i = \frac{\ln\left(A_{\text{sup}-\text{i}}\right) - \ln\left(A_{\text{inf}-\text{i}}\right)}{\omega_n \cdot \left(t_{\text{Ainf}-\text{i}} - t_{\text{Asup}-\text{i}}\right)} \ . \tag{44}$$

The average amplitude for each segment is

$$A_{\text{av,i}} = \frac{A_{\text{sup}-\text{i}} + A_{\text{inf}-\text{i}}}{2} \ . \tag{45}$$

Finally, the damping ratio ξ_i is assigned to the averaged amplitude $A_{\text{av,i}}$ so that the dependence of the damping ratio on the amplitude can be determined.

This process is repeated for all the decays of the series (see Fig. 7). With this, the damping characteristic can be determined as a function of the amplitude for every mode shape of the disk and for every configuration shown in Fig. 3. Fig. 10 shows this trend for the example used in this section. Every circle is associated with one segment of one of the envelopes analyzed. The damping obtained from one segment of the envelope is associated to the averaged amplitude (Eq. (45)). It can be seen that similar amplitudes give similar damping values, which may indicate the dependence of the damping on the amplitude of vibration. It is also interesting to observe the repeatability of the results with respect to the vibration amplitude, no matter the damping is extracted in a segment just when the free decay starts or a segment in the middle of the decay.

Note that the calculated value corresponds to the total damping, which considers the material damping and the structural damping as follows:

$$\boldsymbol{\xi}_{\text{total}} = \boldsymbol{\xi}_{\text{structural}} + \boldsymbol{\xi}_{\text{Material}} + \boldsymbol{\xi}_{\text{Fluid}}. \tag{46}$$

In Eq. (46), structural damping is related to the energy dissipation through the joints and fixings of the structure. Material damping is related to a micro-scale energy dissipation process of the material of the disk during the deformation of the structure. Finally, fluid damping is related to the mechanical energy dissipation in the fluid, mainly by viscous forces.

Structural damping and material damping may be determined for the structure vibrating in air. In air, the contribution of the fluid damping is one or two orders less than in water [23] as such the total damping can be attributed to the structural and material damping in this configuration.

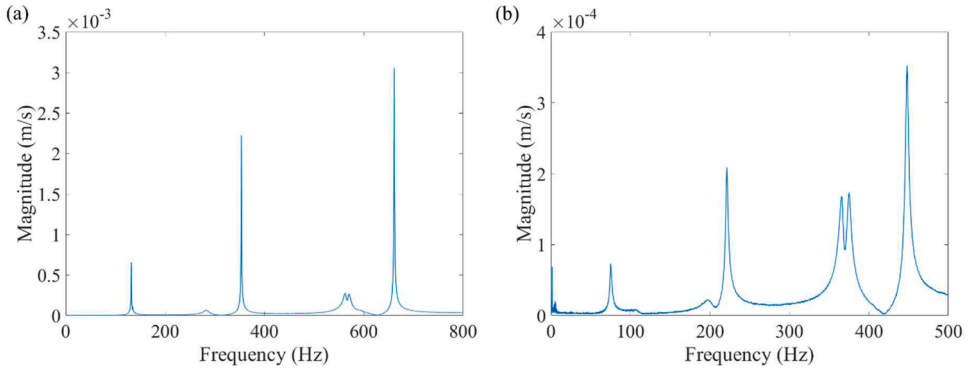


Fig. 12. Spectrums of the configurations: (a) Infinite water (d/D = 47.2 %) and (b) Close to the rigid wall (d/D = 0.8 %).

Table 2
Summary of frequencies for each mode in the different cases.

Case	d (mm)	d/D (%)	fn =2 (Hz)	fn=3 (Hz)	fn=4 (Hz)
Simulation (Vacuum)	–	–	233.22	558.69	981.99
Experimental (Air)	–	–	221.44	552.31	980.19
Experimental (Water)	118	47.2	132.06	353.69	661.56
	18	7.2	122.25	336.94	641.45
	10	4	110.31	310.63	601.88
	5	2	95.19	273.69	540.88
	2	0.8	75.06	221.38	447.63

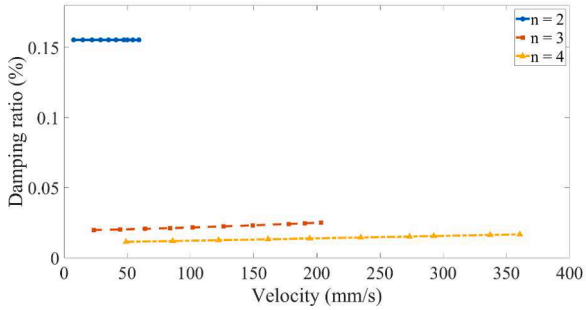


Fig. 13. Damping ratio obtained in the air test for the three vibration modes.

Table 3
Structural and material damping.

Mode	Structural and material damping [%]
$n = 2$	0.155
$n = 3$	0.0199
$n = 4$	0.0115

5. Experimental results

5.1. Identification of the damped frequencies and mode shapes

Firstly, a chirp excitation (5 repetitions) is applied to a freely supported disk surrounded by air. After FFT is applied to the acquired data and the spectrum averages are made, a frequency spectrum with three dominant peaks is obtained, as shown in Fig. 11a.

To determine the vibrating mode, a simple numerical simulation is conducted in the Modal module of ANSYS 2020R2. This simulation is made in a free vibrating condition to be compared with the frequencies obtained experimentally. The $n = 2$, $n = 3$, and $n = 4$ modes of the simulation are shown in Fig. 11b–d with their respective frequency values. Given the small discrepancy between the experimental and numerical frequencies obtained, it can be considered that the first peak of the spectrum (Fig. 11a) corresponds to the

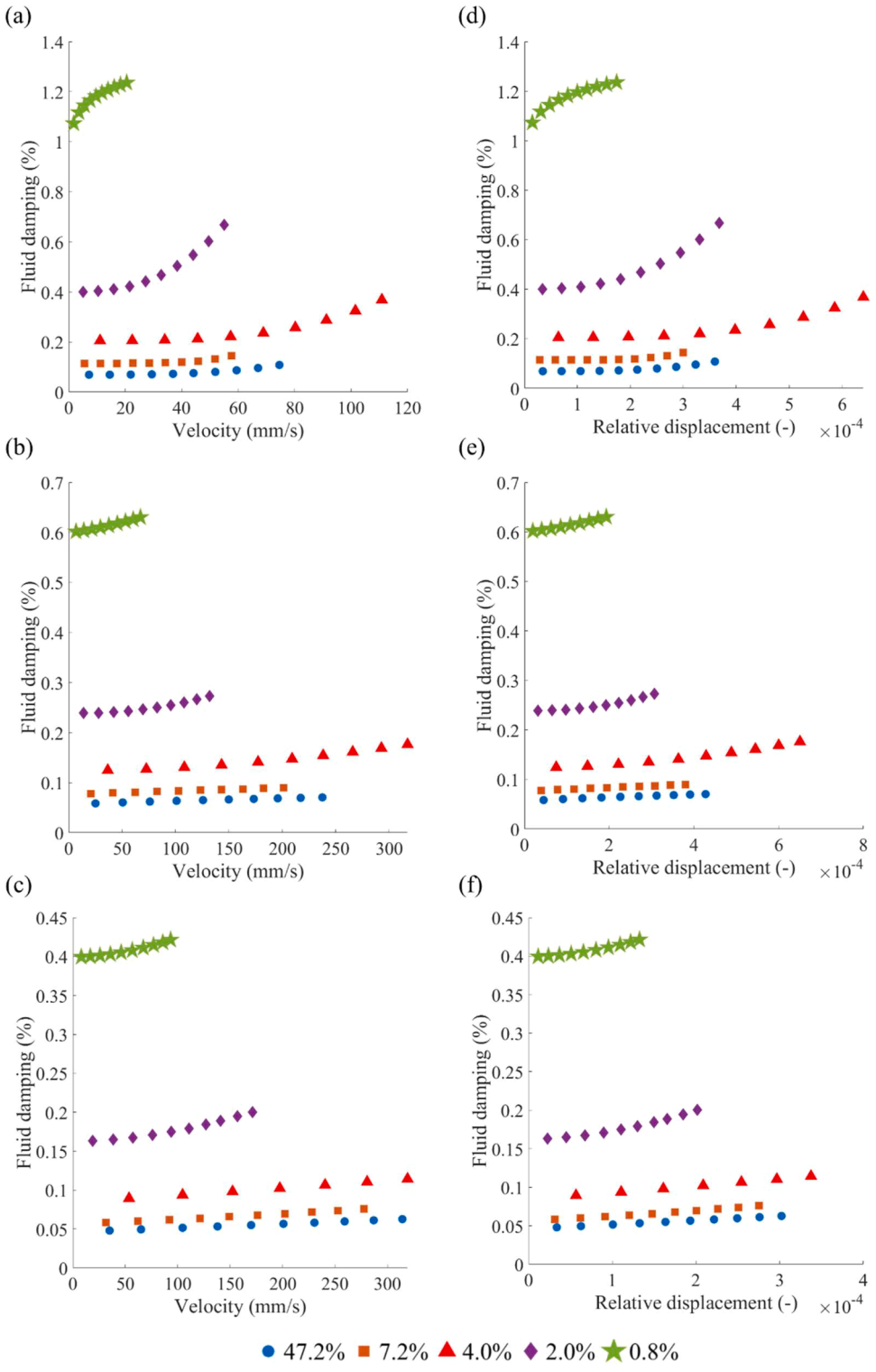


Fig. 14. Fluid damping at different configurations: Fluid damping vs. vibration velocity: (a) $n = 2$, (b) $n = 3$ and (c) $n = 4$. Fluid damping ratio vs. vibration relative displacement: (d) $n = 2$, (e) $n = 3$ and (f) $n = 4$.

mode $n = 2$, the second peak to the mode $n = 3$ and the third peak to the mode $n = 4$. In Fig. 11a, it is possible to see two peaks with low amplitudes in between the peaks of interest. The first one between the mode $n = 2$ and $n = 3$ corresponds to the mode $n = 0$. The second corresponds to the mode $(n, s) = (1, 1)$, which has 1 nodal diameter and 1 nodal circle.

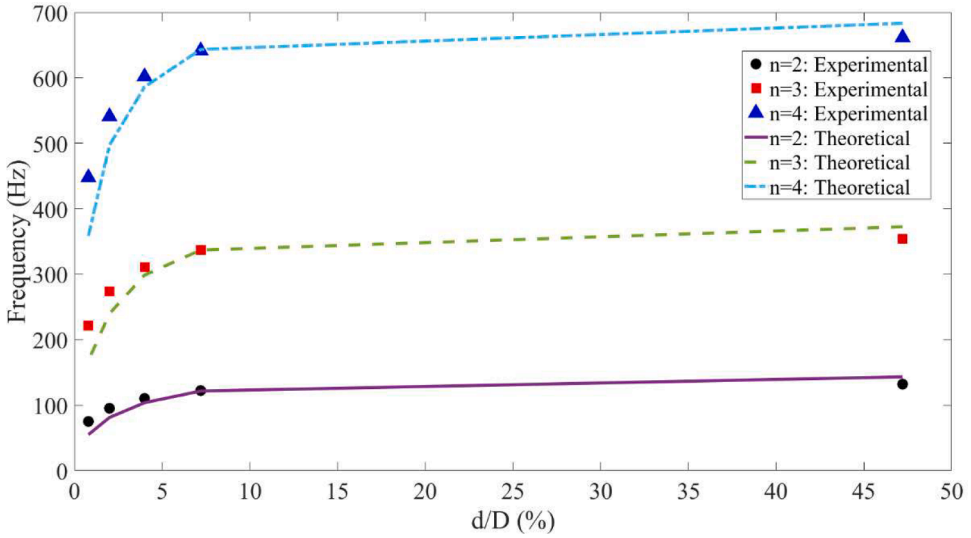


Fig. 15. Analytically and experimentally obtained frequencies at different configurations.

In the response of the disk for infinite water condition (Fig. 12a), the three diametrical modes have decreased the natural frequencies due to the added mass effect. The added mass effect is even larger when the disk gets close to a rigid wall, as described by many authors [28–30] (Fig. 12b).

Table 2 shows the damped frequencies corresponding to the diametrical modes of the disk for all the configurations tested. It can be clearly seen that when the distance disk-rigid wall tends to zero, the damped frequencies greatly decrease due to an increased added mass. The influence of the distance between the disk and the rigid wall on the damped frequencies of the disk is higher when the ratio d/D is less than 10 %. Therefore, most of the tested configurations are under this value.

5.2. *Fluid damping. Influence of the vibration amplitude and distance to the rigid surface*

For every configuration, the damping ratio is determined as a function of the vibration amplitude as explained in Section 3.2. The present study is focused on fluid damping; therefore, the effects of the structural and material damping have to be removed (Eq. (46)). The contribution of the structural and material damping is estimated for the disk vibrating in air with a low amplitude of vibration. In this situation, the contribution of the fluid damping when the structure is vibrating in air is one or two orders of magnitude less than when the structure is vibrating in water. Fig. 13 shows the total damping ratio of the vibrating disk in air. For the lowest vibration amplitude, we may assume that $\xi_{\text{Fluid}} \approx 0$ and therefore, $\xi_{\text{material}} + \xi_{\text{structural}}$ can be extracted. These values for the three vibrating modes are shown in Table 3.

The fluid damping ratios are obtained by extracting the structural and material damping from the total damping calculated with the segments of the free decay. In Fig. 14, each curve of points corresponds to a fixed distance to the rigid wall (d/D). It can be clearly appreciated that the fluid damping increases when the vibration amplitude increases (Fig. 14a–c). Furthermore, damping ratios are higher when the disk is closer to the rigid wall. Finally, the relative variation of the damping with the amplitude of vibration is also higher, i.e. the fluid damping is more affected by the amplitude of vibration for configurations where the disk is closer to the rigid wall. Note that there are some differences in the amplitude range of every configuration. This is because the maximum voltage given to the exciter was always the same (250 V) and the amplitude of resonance is lower for configurations where the damping is higher. Fig. 14d–f shows the same results but for vibration relative displacement (defined as the ratio between the displacement and the diameter of the disk) instead of vibration velocity.

From this figure, three important different observations can be made:

- Lower modes show higher fluid damping ratios.
- Closer distance to the rigid wall induces higher fluid damping.
- The fluid damping depends on the vibration amplitude. This dependence is stronger for closer distances to the rigid wall.

6. Interpretation of the experimental results

In this section we use the analytical model proposed in Section 3 to explain the main experimental results observed.

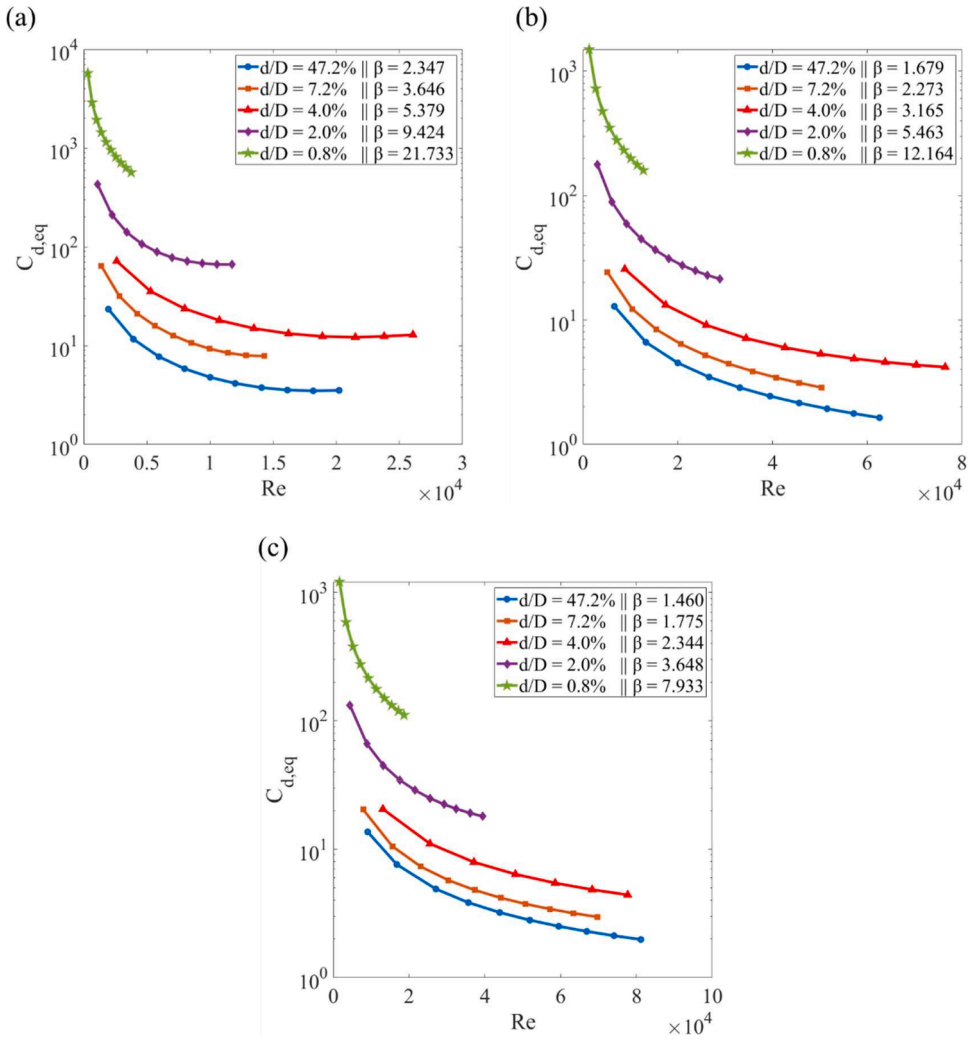


Fig. 16. Equivalent drag coefficients vs. Reynolds number for: (a) $n = 2$, (b) $n = 3$ and (c) $n = 4$.

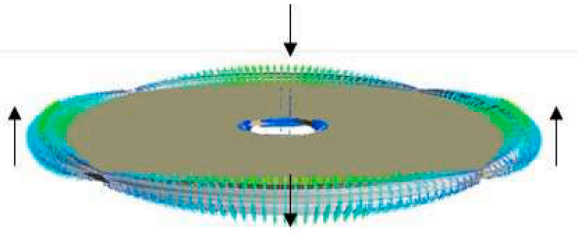


Fig. 17. Edge vortices on a disk vibrating close to a rigid wall.

6.1. *Free vibration frequencies of the submerged disk*

To calculate the free vibration frequencies of the disk at the different configurations, as explained in Sections 2.2 and 2.3, the following values were used: $a = 0.125$ m, thickness $h = 0.003$ m, $E = 2.1\times*10^{11}$ Pa, $\nu = 0.33$, $\rho_D = 7850$ kg/m^3, $\rho_F = 1000$ kg/m^3 and n values from 2 to 4.

The frequencies for every configuration and mode shape are obtained as shown in Fig. 15. The theoretically obtained frequencies are shown and contrasted with the experimental values shown in Table 2. These have been calculated using Eq. (13) once the AVMI factors have been obtained by means of the Eq. (14).

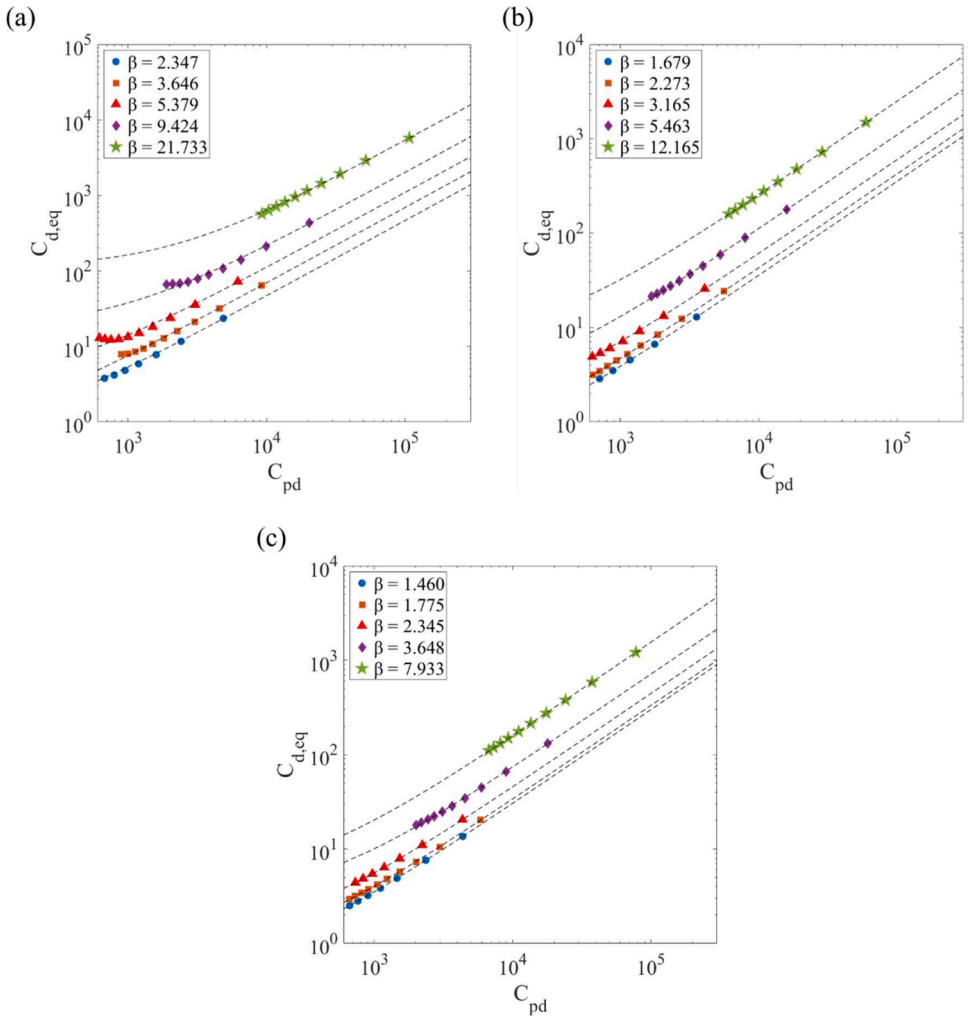


Fig. 18. Equivalent drag coefficient vs. analog drag coefficient based on the pressure difference: (a) $n = 2$, (b) $n = 3$ and (c) $n = 4$.

6.2. *Equivalent drag coefficient*

Blevins [22] used in his model the concept of the drag coefficient C_d to explain the theoretical linear relationship between the damping and the amplitude of an oscillating cylinder in a heavy flow with high Reynolds numbers. In our case, experimental values of the damping are used in Eq. (40) to obtain the equivalent drag coefficients $C_{d,eq}$. These are shown in Fig. 16 with respect to the Reynolds numbers, which is defined as:

$$Re = \frac{\rho_F \omega_{ns} A_n D}{\mu}, \tag{47}$$

where, μ is the dynamic viscosity of the fluid.

The dependance of $C_{d,eq}$ with Re number is clear and it looks similar to the classical C_d with Re for external flows around bodies [35]. From this figure it can be seen that higher AVMI factors β results in higher $C_{d,eq}$ (see Fig. 16) and also in higher damping ratios (see Fig. 14). This observation is consistent with the experimental results of Valentin et al. [23]. Nevertheless, the reason of why this relation holds is not justified in that paper.

To justify this dependance, we propose the following explanation. By increasing the added mass β, the pressure difference in both sides of the disk has to be increased as shown for example by Kubota and Suzuki [30,31] and Presas et al. [36]. This particularly happens for configurations where the disk is close to the wall. Higher pressure differences on the edge of the disk would create more intense vortexes in its periphery and part of the kinetic energy of the fluid is dissipated by these ones, similar to the phenomena of trailing tip vortexes [37]. For illustrating this phenomenon Fig. 17 is obtained from a k-ε CFD model and shows the vorticity at the trailing edge of the disk.

Note that even the pressure distribution in a diametrical mode is symmetric, the energy dissipated in these vortices would add to

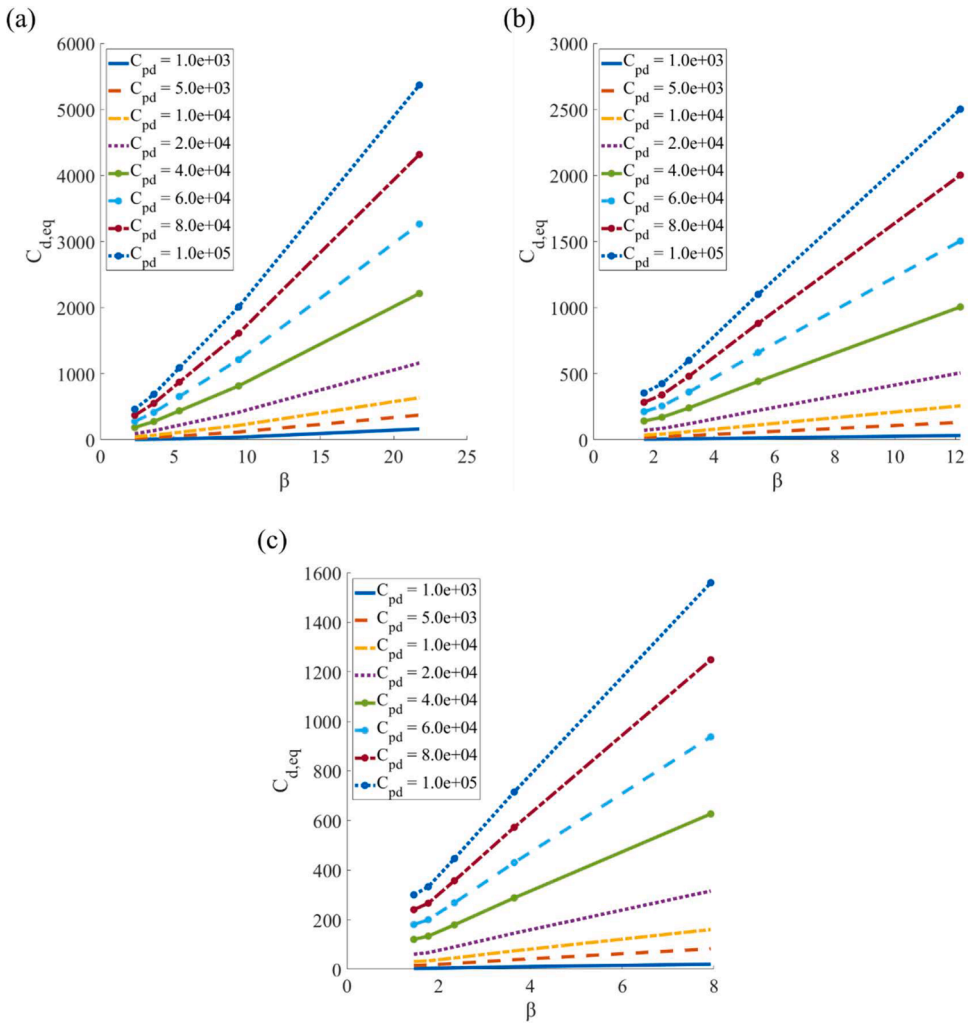


Fig. 19. Equivalent drag coefficient vs AVMI factor at different constant $C_{d,eq}$: (a) $n = 2$, (b) $n = 3$ and (c) $n = 4$.

each other. The dissipation mechanism inside these vortexes may be complicated to be determined analytically, and requires from experimentation or advanced numerical simulation models which may be discussed in future papers. This phenomenon maybe also similar to the observation made in Ref. [24] by Vu et al., where they observed an abrupt increase of the damping ratio when a vibrating plate was causing turbulences.

At this stage, the purpose of the present paper is to characterize the $C_{d,eq}$ with a normalized pressure coefficient C_{pd} which is defined in the following section.

6.3. *Pressure coefficient*

A pressure coefficient is defined as the static pressure applied on the disk surface over the kinetic energy of the fluid in contact with the disk. The pressure field can be derived directly from the velocity potential combined with the non-stationary Bernoulli equation [35]:

$$P = -\rho_F \frac{\partial \varnothing(r,z,t)}{\partial t} \tag{48}$$

Then, the pressure difference between the faces of the disk is given by (see Eqs. (22) and (23) for $\varnothing_{up}$ and $\varnothing_{down}$):

$$\Delta P = -\rho_F \left(\varnothing_{up}|_{z=0} - \varnothing_{down}|_{z=0}\right)\ddot{g}(t) \tag{49}$$

An integration of ΔP in all the disk surface would give zero due to the symmetry of the diametrical modes. Therefore, to calculate an equivalent force of the pressure, only one portion of the area, namely $[-\frac{\pi}{2n}, +\frac{\pi}{2n}]$ is considered. This gives an averaged pressure over the portion of the area:

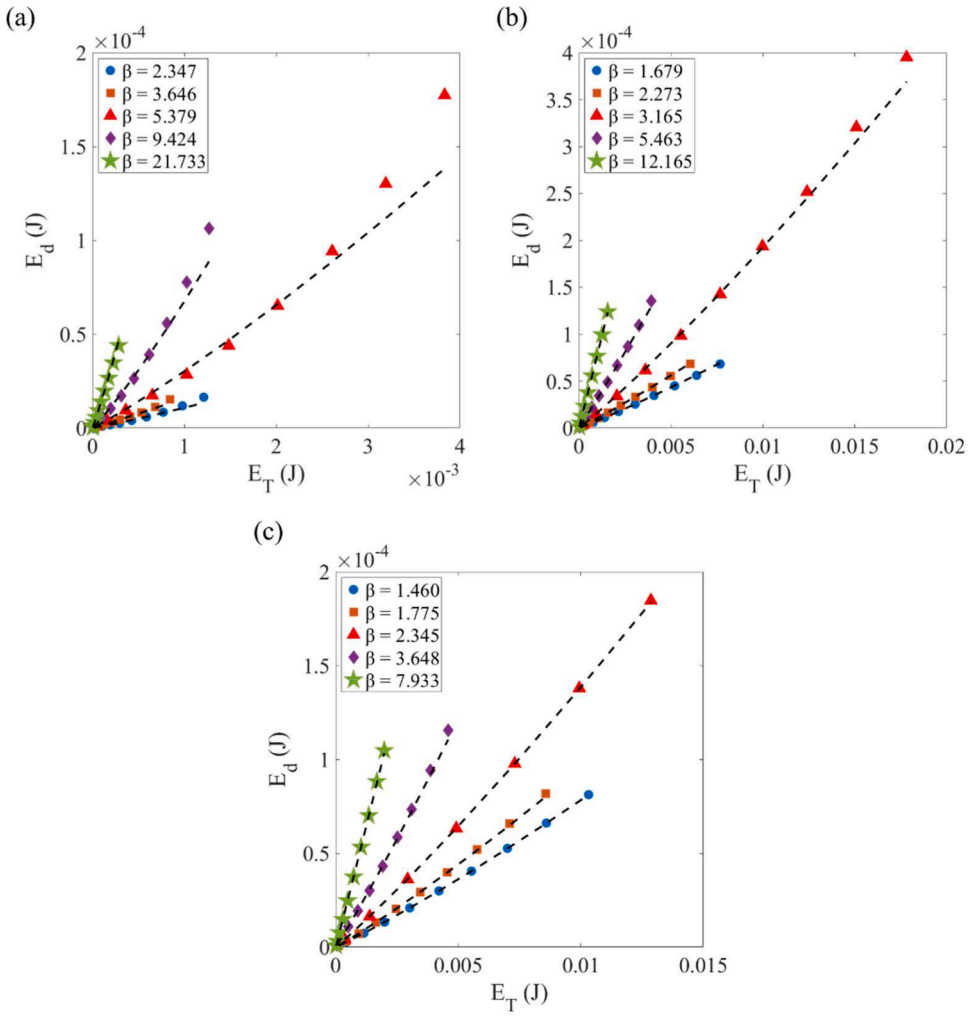


Fig. 20. Dissipated energy vs. total energy of the disk (experimental values in dots and approximated values in dashed lines): (a) $n = 2$, (b) $n = 3$, (c) $n = 4$.

$$\Delta P_n = \int_0^a \int_{\theta 1}^{\theta 2} \Delta P \hat{r} d\theta d\hat{r} \Big/ \left(\frac{a^2}{n}\right)$$
$$with: \theta 1 = -\theta 2 = -\frac{\pi}{2n}, \tag{50}$$

Considering the velocity on the disk surface, the equivalent kinetic energy in the same sector can be calculated as:

$$Q_{p,n} = \frac{1}{2}\rho_F \int_0^a \int_{\theta 1}^{\theta 2} \left(A_n \psi_{r,ns} \psi_\theta \dot{g}(t)\right)^2 \hat{r} d\theta d\hat{r} \Big/ \left(\frac{a^2}{n}\right)$$
$$with: \ \theta 1 = -\theta 2 = -\frac{\pi}{2n}, \tag{51}$$

Finally, the equivalent pressure coefficient C_{pd} can be defined as:

$$C_{pd} = \frac{\Delta P_n}{Q_{p,n}} \tag{52}$$

This coefficient is evaluated at every configuration and amplitude. C_{pd} is contrasted with the equivalent drag coefficient $C_{d,eq}$ in Fig. 16. The different tested configurations are shown in terms of the corresponding AVMI factor obtained for each mode shape.

In Fig. 18 it can be seen a strong correlation between the proposed C_{pd} and $C_{d,eq}$. Note that $C_{d,eq}$ is related to the real energy dissipation and C_{pd} has been derived from the potential flow theory. Regressions obtained in Fig. 18 are represented in a more

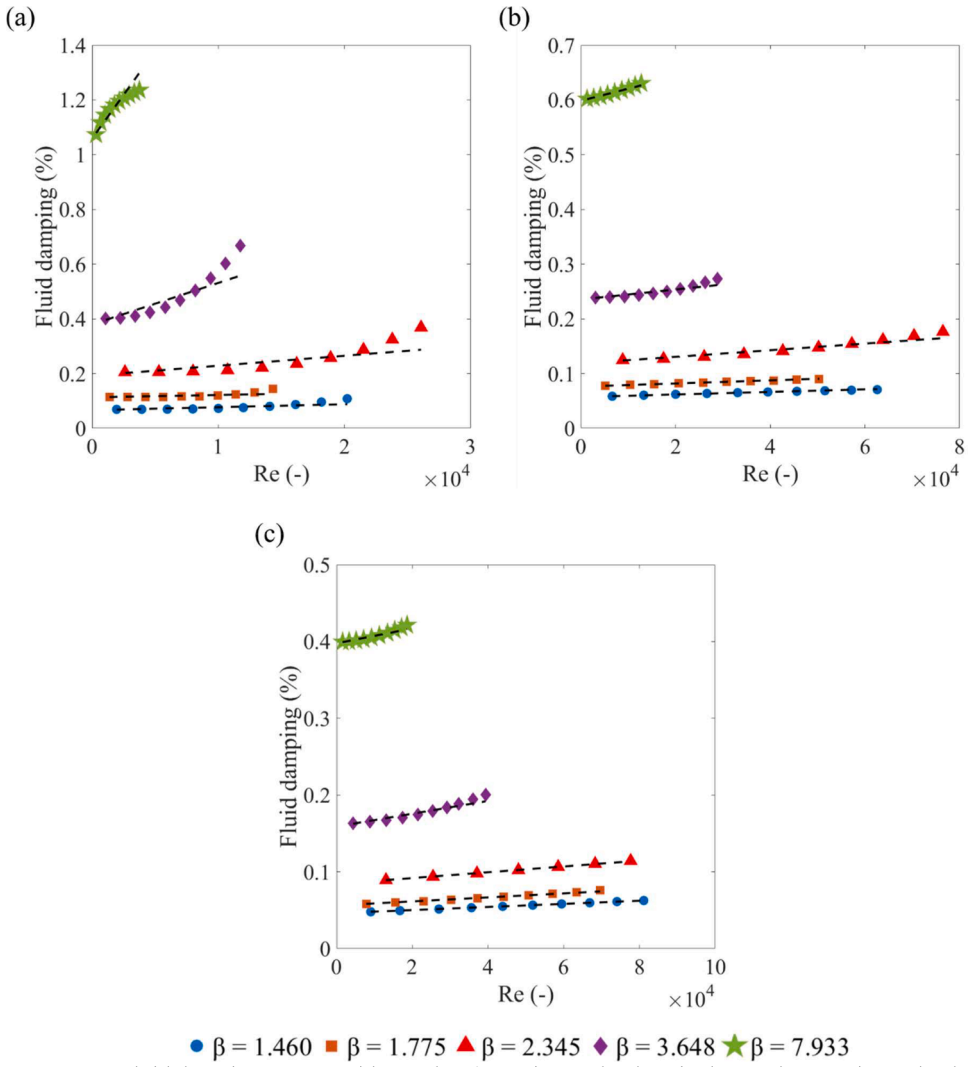


Fig. 21. Fluid damping vs Reynolds number (experimental values in dots and approximated values in dashed lines): (a) $n = 2$, (b) $n = 3$, (c) $n = 4$.

convenient way in Fig. 19, where it can be seen how the $C_{d,eq}$ is highly influenced by the AVMI factor at different constant values of C_{pd}.

The energy dissipated E_d can be calculated based on $C_{d,eq}$ according to Eq. (38). E_d calculated with the regressions of Fig. 19 and calculated based on the experimental results is shown in Fig. 20. It can be seen that the ratio between dissipated energy and the kinetic energy of the disk decreases with the increasing mode shape n.

6.4. Fluid damping

The approximated dissipated energy shown in Fig. 20 can be evaluated in Eq. (1) and the fluid damping ratio is obtained and shown in Fig. 21. In this figure, both experimentally obtained and approximated fluid damping ratios are represented. It can be seen that a good matching between analytical and experimental results is reached. The behavior of the approximated damping ratios has the same features as the ones described in Section 5.2 for experimental results.

7. Conclusions

In this study, the fluid damping of a vibrating disk submerged in water and close to a rigid surface has been experimentally and theoretically analyzed. The disk has been excited with a light PZT and the response has been measured with a Laser Doppler Vibrometer. Accurate estimations of the damping ratio have been obtained by analyzing the free decay response of the disk.

We show that fluid damping increases when the vibration amplitude increases. When the disk is vibrating very close to the rigid wall, higher damping ratios and stronger correlations between the damping and the vibration amplitude are observed.

The highest fluid damping ratios were found for the lowest diametrical mode ($n = 2$). In addition to the damping ratios, the dependence of fluid damping on the vibration amplitude and distance to the rigid wall was also stronger for this mode. On the other hand, fluid damping for the highest diametrical mode ($n = 4$) was the lowest among the 3 modes, and its dependence on the vibration amplitude and distance to the rigid wall was also the weakest one.

The mechanisms of energy dissipation in a viscous fluid are complicated and same as in classical fluid mechanic problems, they need from experimentation for the development of consistent theories. Possible reasons for the fluid damping mechanism have been analytically studied in this paper. In previous studies, it was observed a possible correlation between the added mass factor and the fluid damping, although the reasons of this correlation were not discussed. We propose the hypothesis that strong pressure differences in the two faces of the disk will lead to energy dissipation on peripheral vortexes. These vortexes will be more intense when the disk vibrates close to the rigid wall and the added mass is higher. Finally, we showed that the damping ratio of a disk vibrating close to a rigid wall in a viscous fluid and with different amplitudes could be characterized as a function of the AVMI factor β and a pressure coefficient defined in this paper C_{pd}. These results and characterization should be validated with further experiments and advanced numerical models.

CRediT authorship contribution statement

Greco Moraga: Methodology, Data curation, Writing – original draft, Validation. **Xiang Xia:** Software, Methodology. **Sergi Roig:** Methodology. **Carme Valero:** Supervision. **David Valentín:** Conceptualization, Methodology. **Mònica Egusquiza:** Methodology. **Lingjiu Zhou:** Conceptualization. **Eduard Egusquiza:** Conceptualization, Funding acquisition. **Alexandre Presas:** Conceptualization, Methodology, Writing – review & editing.

Declaration of Competing Interest

The authors declare that they have no known competing financial interests or personal relationships that could have appeared to influence the work reported in this paper.

Data availability

Data will be made available on request.

Acknowledgements

This work was funded by the National Agency for Research and Development (ANID) / Scholarship Program / DOCTORADO BECAS CHILE/2020 - 72210054. Alexandre Presas and David Valentin want to acknowledge the Serra Hunter Program of Generalitat de Catalunya. The authors want to acknowledge Serena Mahnoor for proofreading this work.

References

[1] X.X. Huang, E. Egusquiza, C. Valero, A. Presas, Dynamic behaviour of pump-turbine runner: from disk to prototype runner, IOP Conf. Ser. Mater. Sci. Eng. (2013), https://doi.org/10.1088/1757-899X/52/2/022036.
[2] M. Louyot, B. Nennemann, C. Monette, F.P. Gosselin, Modal analysis of a spinning disk in a dense fluid as a model for high head hydraulic turbines, J. Fluids Struct. 94 (2020), https://doi.org/10.1016/j.jfluidstructs.2020.102965.
[3] M. Amabili, G. Frosali, M.K. Kwak, Free vibrations of annular plates coupled with fluids, J. Sound Vib. 191 (1996) 825–846, https://doi.org/10.1006/jsvi.1996.0158.
[4] C.G. Rodriguez, E. Egusquiza, X. Escaler, Q.W. Liang, F. Avellan, Experimental investigation of added mass effects on a Francis turbine runner in still water, J. Fluids Struct. 22 (2006) 699–712, https://doi.org/10.1016/j.jfluidstructs.2006.04.001.
[5] R. Lagrange, Y. Fraigneau, New estimations of the added mass and damping of two cylinders vibrating in a viscous fluid, from theoretical and numerical approaches, J. Fluids Struct. 92 (2020), 102818, https://doi.org/10.1016/j.jfluidstructs.2019.102818.
[6] C. Conca, A. Osses, J. Planchard, Added mass and damping in fluid-structure interaction, Comput. Methods Appl. Mech. Eng. 146 (1997) 387–405, https://doi.org/10.1016/S0045-7825(96)01246-7.
[7] C.G. Rodriguez, P. Flores, F.G. Pierart, L.R. Contzen, E. Egusquiza, Capability of structural-acoustical FSI numerical model to predict natural frequencies of submerged structures with nearby rigid surfaces, Comput. Fluids 64 (2012) 117–126, https://doi.org/10.1016/j.compfluid.2012.05.011.
[8] E. Askari, K.H. Jeong, M. Amabili, Hydroelastic vibration of circular plates immersed in a liquid-filled container with free surface, J. Sound Vib. 332 (2013) 3064–3085, https://doi.org/10.1016/j.jsv.2013.01.007.
[9] J. Li, Y. Qu, Y. Chen, H. Hua, Investigation of added mass and damping coefficients of underwater rotating propeller using a frequency-domain panel method, J. Sound Vib. 432 (2018) 602–620, https://doi.org/10.1016/j.jsv.2018.06.060.
[10] Y. Yadykin, V. Tenetov, D. Levin, The added mass of a flexible plate oscillating in a fluid, J. Fluids Struct. 17 (2003) 115–123, https://doi.org/10.1016/S0889-9746(02)00100-7.
[11] C.-C. Liang, Y.S. Tai, P.L. Li, Natural frequencies of annular plates having contact with fluid, J. Sound Vib. 228 (1999) 1167–1181, https://doi.org/10.1006/jsvi.1999.2463.
[12] C.-C. Liang, C.-C. Liao, Y.-S. Tai, W.-H. Lai, The free vibration analysis of submerged cantilever plates, Ocean Eng. 28 (2001) 1225–1245, https://doi.org/10.1016/S0029-8018(00)00045-7.
[13] P. Dörfler, M. Sick, A. Coutu, Flow-Induced Pulsation and Vibration in Hydroelectric Machinery, Springer, 2013, https://doi.org/10.1007/978-1-4471-4252-2. London.
[14] J. Yang, X. Tian, X. Li, Hydrodynamic characteristics of an oscillating circular disk under steady in-plane current conditions, Ocean Eng. 75 (2014) 53–63, https://doi.org/10.1016/j.oceaneng.2013.11.011.

[15] A. Abazari, M. Behzad, K. Thiagarajan, Hydrodynamic damping enhancement by implementing a novel combined rigid-elastic heave plate, J. Mar. Sci. Technol. 26 (2021) 216–232, https://doi.org/10.1007/s00773-020-00732-7.
[16] M.J. Rao, S. Nallayarasu, S.K. Bhattacharyya, Numerical and experimental studies of heave damping and added mass of spar with heave plates using forced oscillation, Appl. Ocean Res. 111 (2021), https://doi.org/10.1016/j.apor.2021.102667.
[17] K.H. Vu, B. Chenu, K.P. Thiagarajan, Hydrodynamic damping due to porous plates, in: Proceedings of the WSEAS International Conference on Fluid Mechanics, Corfu, 2004, pp. 17–19.
[18] S. Ann, O.M. Faltinsen, An experimental and numerical study of heave added mass and damping of horizontally submerged and perforated rectangular plates, J. Fluids Struct. 39 (2013) 87–101, https://doi.org/10.1016/j.jfluidstructs.2013.03.004.
[19] J.P. Gauthier, A.M. Giroux, S. Etienne, F.P. Gosselin, CFD evaluation of added damping due to fluid flow over a hydroelectric turbine blade, IOP Conf. Ser. Earth Environ. Sci. (2016), https://doi.org/10.1088/1755-1315/49/7/072003. Institute of Physics Publishing.
[20] W. Wang, L. Zhou, X. Xia, R. Tao, Analysis of the hydrodynamic damping characteristics on a symmetrical hydrofoil, Renew. Energy 178 (2021) 821–829, https://doi.org/10.1016/j.renene.2021.06.026.
[21] S. Roth, M. Calmon, M. Farhat, C. Muench, B. Huebner, F. Avellan, P. Rudolf, Hydrodynamic damping identification from an impulse response of a vibrating blade, in: Proceedings of the 3rd IAHR International Meeting of the Workgroup on Cavitation and Dynamic Problems in Hydraulic Machinery and Systems, Brno, Czech Republic, Brno University of Technology, 2009, pp. 253–260.
[22] R.D. Blevins, Flow-Induced Vibration, Van Nostrand Reinhold, 1977. New York.
[23] D. Valentín, A. Presas, E. Egusquiza, C. Valero, Experimental study on the added mass and damping of a disk submerged in a partially fluid-filled tank with small radial confinement, J. Fluids Struct. 50 (2014) 1–17, https://doi.org/10.1016/j.jfluidstructs.2014.06.006.
[24] V.H. Vu, M. Thomas, A.A. Lakis, L. Marcouiller, Effect of added mass on submerged vibrated plates, in: Proceedings of the 25th Seminar On Machinery Vibration, Canadian Machinery Vibration Association, 2007. St John, NBNB40.1-40.15.
[25] S.K. Nayak, K.C. Biswal, Fluid damping in rectangular tank fitted with various internal objects - An experimental investigation, Ocean Eng. 108 (2015) 552–562, https://doi.org/10.1016/j.oceaneng.2015.08.042.
[26] C. Atkinson, M. Manrique de Lara, Fluid reaction on a vibrating disc in a viscous medium, Int. J. Eng. Sci. 44 (2006) 973–995, https://doi.org/10.1016/j.ijengsci.2006.05.009.
[27] J.M. Génevaux, N. Dauchez, O. Doutres, Nonlinear damping of a plate using Faraday instability of a fluid film, J. Sound Vib. 326 (2009) 150–160, https://doi.org/10.1016/j.jsv.2009.04.038.
[28] A.W. Leissa, Vibration of plates, scientific and technical information division, National Aeronautics and Space Administration, 1969. Washington.
[29] M.K. Kwak, S.A. And, K.C. Kim, Axisymmetric vibration of circular plates in contact with fluid, J. Sound Vib. 146 (1991) 381–389, https://doi.org/10.1016/0022-460X(91)90696-H.
[30] Y. Kubota, T. Suzuki, Added mass effect on disc vibrating in fluid, Trans. Jpn. Soc. Mech. Eng. C 50 (1984) 243–248.
[31] Y. Kubota, H. Ohashi, A study on the natural frequencies of hydraulic pumps, in: Proceedings of the 1st ASME Joint International Conference on Nuclear Engineering, 1991, pp. 589–593.
[32] M. Amabili, Effect of finite fluid depth on the hydroelastic vibrations of circular and annular plates, J. Sound Vib. 193 (1996) 909–925, https://doi.org/10.1006/jsvi.1996.0322.
[33] R.D. Blevins, Flow-Induced Vibration, 2nd Edition, Krieger, 1990. Malabar.
[34] D.G. Stephens, M.A. Scuvuzzo, Investigation of air damping of circular and rectangular plates, a cylinder, and a sphere, National Aeronautics and Space Administration, Langley Research Center, 1965. Washington D.C.
[35] F.M. White, Fluid Mechanics, 8th ed, McGraw Hill Education, 2016. Secacus, United State.
[36] A. Presas, D. Valentin, E. Egusquiza, C. Valero, U. Seidel, Influence of the rotation on the natural frequencies of a submerged-confined disk in water, J. Sound Vib. 337 (2015) 161–180, https://doi.org/10.1016/j.jsv.2014.10.032.
[37] M.J. Ringuette, M. Milano, M. Gharib, Role of the tip vortex in the force generation of low-aspect-ratio normal flat plates, J. Fluid Mech. 581 (2007) 453–468, https://doi.org/10.1017/S0022112007005976.